Environmental Science and Ecotechnology 10 (2022) 100168

Contents lists available at ScienceDirect

Environmental Science and Ecotechnology

journal homepage: www.journals.elsevier.com/environmental-science-and-ecotechnology/

Original Research

Tailoring a novel hierarchical cheese-like porous biochar from algae residue to boost sulfathiazole removal

Ke Wang [a], Yue Wang [a], Shiyu Zhang [a], Yi-di Chen [a, b], Rupeng Wang [a], Shih-Hsin Ho [a, *]

[a] State Key Laboratory of Urban Water Resource and Environment, School of Environment, Harbin Institute of Technology, Harbin, 150040, PR China
[b] State Key Laboratory of Urban Water Resource and Environment, School of Civil and Environmental Engineering, Harbin Institute of Technology (Shenzhen), Shenzhen, 518055, PR China

ARTICLE INFO

Article history:
Received 27 December 2021
Received in revised form
3 March 2022
Accepted 3 March 2022

Keywords:
Algae residue
Cheese-like porous biochar
Sulfathiazole
$KHCO_3$-activated
Adsorption mechanism

ABSTRACT

Aquatic pollution caused by antibiotics poses a significant threat to human health and the ecosystem. Inspired from "Emmental Cheese" that owns lots of natural pores, we here fabricated a hierarchical cheese-like porous *Spirulina* residue biochar (KSBC) activated by $KHCO_3$ for efficiently boosting the removal of sulfathiazole (STZ). Through learning form nature that the CO_2 produced by bacteria can serve as the natural pore maker (like cheese-making), $KHCO_3$ was thus selected as the gas generating agent in this study. The effect of adding $KHCO_3$ on the surface properties of KSBC was comprehensively investigated. Benefiting from the activation, the KSBC with the mass ratio of 2:1 (2K-SBC) possessed the largest specific surface areas (1100 $m^2\ g^{-1}$), which was approximately 81 times that of the original (not activated) *Spirulina* residue biochar (SBC) (13.56 $m^2\ g^{-1}$). Moreover, 2K-SBC exhibited the maximum adsorption capacity for STZ (218.4 mg g^{-1}), dramatically higher than the SBC (25.78 mg g^{-1}). The adsorption kinetics and adsorption isotherms exhibited that the adsorption behavior of 2K-SBC for STZ was consistent with the pseudo-second-order and Langmuir models. Additionally, the adsorption thermodynamics revealed that the adsorption of STZ on 2K-SBC was spontaneous and exothermic. The pore-filling and electrostatic interaction were considered the main mechanism for the adsorption of STZ on 2K-SBC, whereas the π-π electron donor-acceptor (EDA) interaction and hydrogen bond would also partially contribute to the adsorption process.

1. Introduction

In recent years, the increasingly serious problem of antibiotic contamination has caused widespread concern worldwide [1–3]. Antibiotics leaked into the environment accumulate through the food chain and harm humans [4,5]. As a member of sulfonamide antibiotics, sulfathiazole (STZ) has been widely detected in natural waters [6]. Nowadays, the increasing content of STZ in water bodies worldwide has posed a critical threat to the ecosystem. Therefore, developing efficient STZ removal systems from water bodies is urgently needed.

Several treatment technologies, including advanced oxidation, electrochemical oxidation, biodegradation, and adsorption, have been extensively employed in treating antibiotics in water environments [7–10]. Among them, adsorption stands out due to its simple process, high efficiency, low cost, and non-toxic intermediates [11]. Compared with metal-containing adsorbents, carbonous materials such as activated carbon, carbon nanotubes, graphene, and biochar have become a research focus in the field of adsorption due to their non-toxicity and absence of secondary pollution during treatment [12–15]. However, the shortcomings of activated carbon, such as unaccepted production cost and complex regeneration, severely limit its practical applicability [16]. Although carbon nanotubes and graphene are also effective in adsorbing pollutants from water bodies, their fabrication processes are relatively cumbersome and cost-intensive, making them difficult to be produced on a mass scale [17,18]. In order to resolve this issue, the use of biochar with a porous structure and high specific surface area may help remove a variety of inorganic and organic pollutants from water bodies and, therefore, represents an excellent potential for its application to treating water bodies [19].

* Corresponding author.
E-mail address: stephen6949@hit.edu.cn (S.-H. Ho).

https://doi.org/10.1016/j.ese.2022.100168

Given this, converting the hazardous algal residue into porous biochar to efficiently adsorb antibiotics in water bodies could simultaneously help reuse the solid waste and eliminate environmental pollution. Recently, to obtain the enhanced adsorption performance for targeted pollutants, various activation methods that can improve the structure and surface properties of biochar have been introduced [20,21]. In this regard, KOH and $ZnCl_2$ are the most widely used activators [22]. However, various challenges such as strong corrosiveness and potential heavy metal leakage are troublesome and can substantially damage the pipelines in practical applications. More importantly, although the increase in micropores in biochar, activated by KOH or $ZnCl_2$, is positively correlated to the adsorption capacity [23,24], the insufficient number of mesopores would limit the mass transfer of pollutant molecules, resulting in a relatively slow adsorption rate [25]. Therefore, seeking out a green environment-friendly activator that can simultaneously make the micropore- and mesopore-rich structured biochar is importance. Fortunately, thanks to the inspiration from the cheese-making process, the authors of the current work believe that $KHCO_3$ may act as an ideal candidate because much of CO_2 thermally generated from $KHCO_3$ can serve as the natural pore maker.

Herein, the high-salted *Spirulina* residue is used as the feedstock as well as the activator, whereas the *Spirulina* residue biochar (SBC) and $KHCO_3$-activated SBC (KSBC) are prepared for efficient removal of STZ. The effect of different amounts of $KHCO_3$ on the structural properties of SBC and the adsorption performance for STZ is systematically investigated. The effects of contact time, initial aqueous pH, inorganic anions, and natural organic matter on the adsorption performance of KSBC have also been explored in detail. This study provides a novel idea for designing a cheese-like biochar-based adsorbent by using hazardous algal residue associated with facial structural activation.

2. Material and methods

2.1. Materials

After extracting phycocyanin, *Spirulina* residue was collected from the East Algae Factory in Fuzhou, Fujian Province, China. The way of phycocyanin extraction provided by the factory was as follows: 50 kg *Spirulina* dry algae powder was added into 1200 kg water. During the dissolution, the temperature was controlled below 18 °C with additions of 20–30 kg calcium chloride, 3–5 kg citric acid, and 20 mL sodium hypochlorite. The mixture was first stirred for 3–5 h and maintained for 8 h, then 15–20 kg of disodium hydrogen phosphate was added and stirred for another 12 h to yield phycocyanin and *Spirulina* residues. Sulfathiazole (STZ, 98%), sodium hydroxide (NaOH, $\geq$ 98%), hydrochloric acid (HCl, 37%), sodium chloride (NaCl, $\geq$ 99.5%), and potassium bicarbonate ($KHCO_3$, 99.5%) were acquired from Sinopharm Chemical Reagent Co., Ltd (Shanghai, China).

2.2. Preparation and characterization of $KHCO_3$-activated SBC (KSBC)

Firstly, the dried *Spirulina* residue was pre-carbonized at 400 °C for 2 h under a N_2 atmosphere to form elementary SBC. Subsequently, various mixtures of $KHCO_3$ and elementary SBC with different mass ratios (0.5:1, 1:1, 2:1, and 4:1) were fully ground in a mortar and carbonized at 800 °C for 2 h under a N_2 environment to form cheese-like KSBC. The heating rate for the above two steps of carbonization was 5 °C min^{-1}. Finally, SBC was washed several times with HCl (1 mol L^{-1}) and deionized water until the filtrate was neutral. Moreover, KSBC samples with different mass ratios were labeled as 0.5K-SBC, 1K-SBC, 2K-SBC, and 4K-SBC, respectively. In addition, SBC without $KHCO_3$ was employed as a reference.

2.3. Batch experiments

First, for the adsorption experiments, 35 mL sulfathiazole (STZ) solution (50 mg L^{-1}) and 17.5 mg SBC/KSBC were placed in a 50 mL conical flask. The conical flask was sealed with sealing film, and the constant temperature water bath oscillator was set to 25 °C. A disposable syringe equipped with 0.22 μm filtration membrane was used to suck 1 mL of the reaction solution during the experiment. Then, the obtained reaction solution was injected into a 1.5 mL brown chromatographic vial for determining the concentration. Different sampling times (1, 3, 5, 10, 15, 20, 30, 60, 90, 120, 180, and 240 min) and different concentrations (50–200 mg L^{-1}) of STZ were used to study the adsorption kinetics and the adsorption isotherms, respectively. Different pH values (3.00, 5.00, 7.00, 9.00, and 11.00) were used to investigate the sensitivity of adsorbents to pH during the adsorption. Different concentrations of humic acid (HA; 1, 5, 10, 20, 30, and 50 mg L^{-1}) and different anions (SO_4^{2-}, Cl^-, NO_3^-, NH_4^+, and CO_3^{2-}) with different concentrations (0.2, 2, and 20 mmol L^{-1}) were adopted to simulate the influence of external factors on the adsorption performance. Other circumstantial experimental details are provided in the *Supplementary Material*.

3. Results and discussion

3.1. Characterization

Specific surface area (SSA), pore volume, and pore size distribution are key indicators for evaluating the adsorption performance of an adsorbent [26,27]. The data presented in Table S1 shows that SSA of SBC was 13.56 m^2 g^{-1}, while that of KSBC increased significantly, attaining a maximum value of 1100 m^2 g^{-1} (2K-SBC) and a lowest of 484.4 m^2 g^{-1} (0.5K-SBC). The increased SSA was conducive to the contact between KSBC and STZ molecules, which benefits the adsorption reaction. Meanwhile, compared with SBC, the total pore volume of KSBC increased significantly, which is consistent with the increase in SSA. However, the average pore sizes of all KSBCs were lower than that of SBC, while the pore volumes of all KSBCs were greater than that of SBC, which suggested that the increased pores were mainly the micropores. Moreover, the increase in micropores was conducive to the increase in adsorption capacity [25,27]. Notably, compared with 2K-SBC, the SSA and total pore volume of 4K-SBC decreased, indicating that excessive $KHCO_3$ was not favorable for the formation of pores. This could be because the impact erosion of excessive $KHCO_3$ on the carbon skeleton was dramatically severe and may lead to serious fragmentation of partial structure, due to which the system became incapable of forming a more complete pore structure. Additionally, as shown in Fig. 1a, all KSBCs exhibited rapid N_2 adsorption at lower relative pressures, suggesting the presence of micropores. Under moderate relative pressures, the BET isotherms of all KSBCs had an apparent hysteretic loop, implying the presence of mesopores. The shapes of all the adsorption and desorption isotherms of KSBCs were in line with Type IV isotherms [28,29]. Moreover, the existence of abundant mesopores and micropores in 2K-SBC was further confirmed by the pore size distribution (Fig. 1b). The existence of mesopores could promote the migration of pollutants in aqueous solutions, which is beneficial to the adsorption of smaller-sized antibiotics, while the existence of micropores could increase the number of adsorption sites [30], indicating that 2K-SBC could be used as a potential adsorbent for STZ.

The surface morphology and microstructure were characterized using scanning electron microscopy (SEM). As displayed in Fig. S1 and

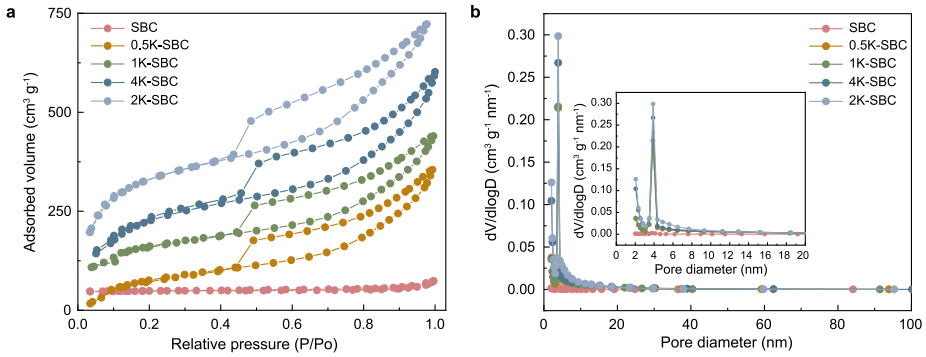

Fig. 1. BET isotherms (**a**) and pore size (**b**) distribution of SBC and KSBC.

Fig. 2, SBC showed an obvious random agglomerate structure, while KSBC exhibited a cheese-like porous structure with a rougher surface. When $KHCO_3$ was used as a pore-forming agent in high-temperature pyrolysis, it would be thermally decomposed to produce a large amount of CO_2 gas. Under high temperatures, the CO_2 gas escaped outwardly and impacted the internal structure of SBC, resulting in the formation of honeycomb and porous structure of KSBC. The phenomenon can be explained using Reaction Equations (1)–(5).

$$2KHCO_3 \rightarrow K_2CO_3 + CO_2 + H_2O \quad (1)$$

$$K_2CO_3 \rightarrow CO_2 + K_2O \quad (2)$$

$$K_2CO_3 + 2C \rightarrow 2K + 3CO \quad (3)$$

$$K_2O + 2C \rightarrow 2K + CO \quad (4)$$

$$CO_2 + C \rightarrow 2CO \quad (5)$$

In addition, the honeycomb porous structure was positively correlated with the amount of $KHCO_3$, which may tremendously promote the adsorption of STZ.

The X-ray diffraction (XRD) patterns were used to analyze the crystal phase of the carbon material before and after the activation. As observed in Fig. 3a, $KHCO_3$ activation had a great influence on the crystal phase. The pattern of peaks in SBC tended to be sharper, representing the presence of numerous crystals. The peak of KSBC was more inclined towards the steamed bread peak, indicating that KSBC was standard amorphous material. Accordingly, the main inorganic salts in SBC were phosphate $Ca_5(PO_4)_3$ and $Ca_2P_2O_7$ with different Ca^{2+} crystal structure sites [31]. This phenomenon represents a lot of inorganic salts that remained on the algal residue after the extraction of phycocyanin. The KSBC spectrum shows that a diffraction peak appeared at 26.34°, which could be attributed to the formation of graphitic carbon from KSBC [32]. Compared with SBC, the CO_2 formed by $KHCO_3$ under high temperature reacted with phosphate, which greatly reduced the phosphate content in KSBC, thus significantly decreasing the calcium salt in the system.

The characteristic chemical bonds and surface functional groups of SBC and $KHCO_3$-activated SBC were further analyzed using Fourier Transform Infrared (FT-IR). As shown in Fig. 3b, the infrared characteristic peak positions of SBC and KSBC were basically the same. Further analysis showed that both the SBC and KSBC had

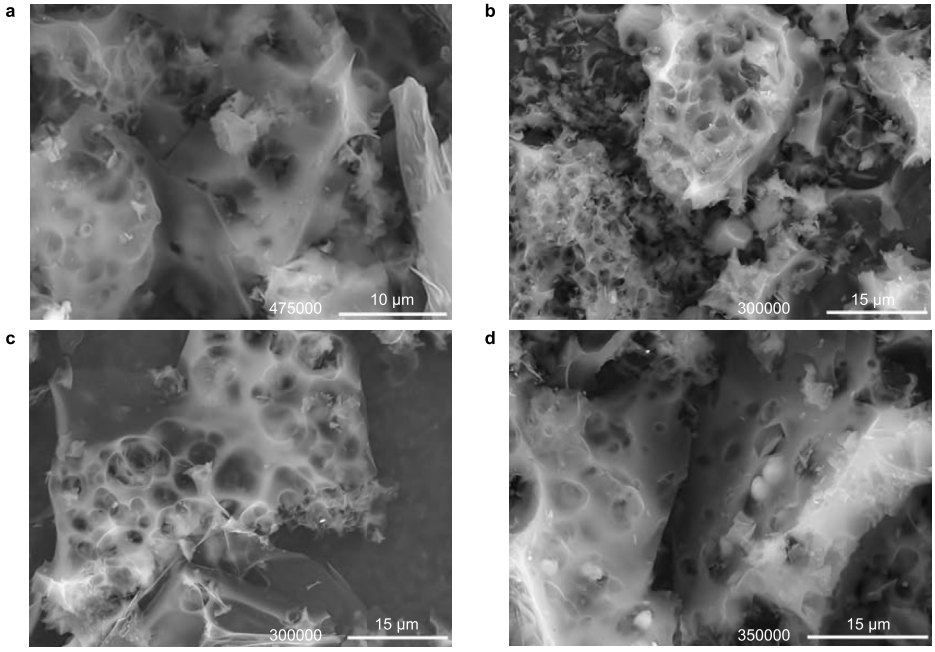

Fig. 2. SEM images of the 0.5K-SBC (**a**), 1K-SBC (**b**), 2K-SBC (**c**), and 4K-SBC (**d**), respectively.

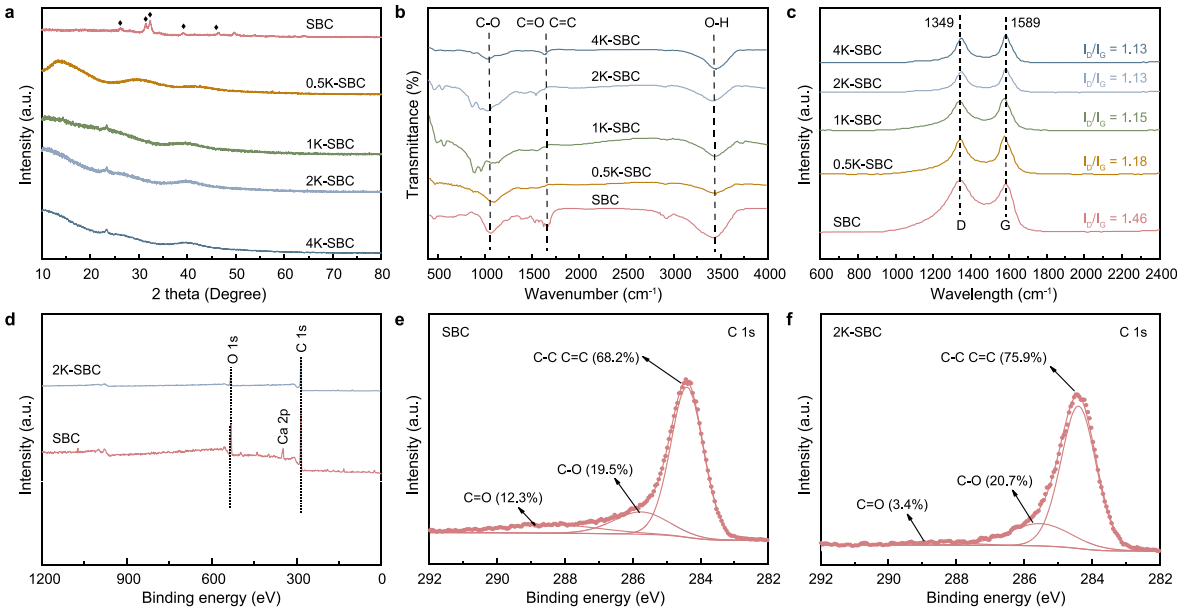

Fig. 3. XRD pattern (**a**), FT-IR spectra (**b**), Raman spectrum (**c**), XPS survey (**d**), and deconvoluted C1s spectra (**e**-**f**) of the SBC and KSBC.

absorption peaks at 1108, 1625, and 3441 cm^{-1}, which belonged to C—O, C═C/C═O, and O—H characteristic absorption bands, respectively [33,34]. Notably, the peak intensities of O—H, C—O, and C═O of KSBC declined, indicating that the activator would reduce the content of oxygen-containing functional groups.

Raman spectroscopy was used to reveal the surface defect state and the degree of graphitization of SBC and $KHCO_3$—activated SBC. As shown in Fig. 3c, the two peaks at 1349 and 1589 cm^{-1} were assigned to D and G bands, respectively. Moreover, D band is related to defects in carbon material, while G band represents its graphitized structure. The ratio (I_D/I_G) can illustrate the degree of graphitization [35,36]. After the activation, the I_D/I_G value of KSBC was not much different. However, all the I_D/I_G values of KSBCs were smaller than that of SBC, indicating that the activation using $KHCO_3$ was beneficial to form a more graphitized structure. In addition, the electrochemical impedance spectroscopy (EIS) could indirectly illustrate the degree of graphitization, and the corresponding results are shown in Fig. S2. The Nyquist diameter of 2K-SBC was significantly smaller than that of SBC, displaying that the activator could increase the degree of graphitization of SBC, thereby enhancing the electron transfer capability [37,38]. Overall, the results showed that the degree of graphitization of SBC could be improved through activation using $KHCO_3$.

The surface elemental composition and chemical states of SBC and 2K-SBC were analyzed using X-ray photoelectron (XPS). As shown in Fig. 3d, SBC and 2K-SBC exhibited clear C1s and O1s peaks at 284.8 and 530.1 eV, respectively. Different from SBC, the peak height of O1s peak in 2K-SBC was lower, indicating that the oxygen content in the activated SBC was reduced. In addition, no Ca 2p peak was observed in 2K-SBC, which might be due to the doping of alkaline $KHCO_3$ pore-forming agent that reacted with the original calcium salt in SBC, thus reducing the content of calcium element. The high-resolution C 1s XPS spectra of SBC and 2K-SBC were successfully resolved into three peaks (Fig. 3e-f) at 284.6, 285.4, and 288.6 eV, which were assigned to C—C/C═C, C—O, and C═O functional groups, respectively [39,40]. However, the percentages of C—C/C═C and C—O/C═O of SBC and 2K-SBC were different from each other. Compared with SBC, the C—C/C═C of 2K-SBC increased from 68.2% to 75.9%, while the overall content of C—O/C═O decreased from 29.8% to 22.1%, which further confirmed that $KHCO_3$ would increase the degree of graphitization and decrease the content of the oxygen functional group [38].

3.2. Effect of contact time, pH, electrolyte ions, and HA on the adsorption of STZ

The effect of reaction time on the adsorption of STZ in the aqueous solution using original SBC and $KHCO_3$-activated SBC was explored. As displayed in Fig. 4a, KSBC adsorbed STZ rapidly within the first 60 min, after which the adsorption rate gradually decreased until achieving equilibrium in 240 min. In comparison, SBC showed the poorest adsorption capacity, indicating the requirement of $KHCO_3$ activation. Interestingly, among all the KSBCs, 2K-SBC exhibited the best adsorption capacity, which may have been due to the following reasons: (1) when the mass ratio ($KHCO_3$ to SBC) was below 2 (for 0.5K-SBC, 1K-SBC, and 2K-SBC), the degree of activation of SBC improved with the increase in the amount of $KHCO_3$, which was mainly due to the increase in SSA and pore volume; (2) once this mass ratio increased to 4 (for 4K-SBC), excessive $KHCO_3$ would strongly impact the carbon skeleton of SBC and cause severe damage on the partial structure, which was mainly manifested in the reduction of SSA and pore volume. As displayed in Fig. S3a, when the concentration of STZ was less than 50 mg L^{-1}, the removal rate of STZ by 2K-SBC was as high as 95%, which continued to increase with the concentration of STZ until the value of 200 mg L^{-1}. After that, the removal rate of STZ dropped by about 20%, indicating that 2K-SBC was suitable for treating STZ wastewater containing less than 50 mg L^{-1} STZ. Therefore, the highest concentration of STZ suitable for 2K-SBC treatment was selected as the research object. As shown in Fig. S3b, when the concentration of 2K-SBC lay within the range of 0.1–0.5 mg L^{-1}, the removal efficiency of STZ increased with the increase in the concentration of 2K-SBC. With a further increase in the concentration of 2K-SBC, the removal efficiency of STZ did not improve significantly. Therefore, considering the amount of 2K-SBC and the removal efficiency of STZ, the concentration of 2K-SBC was regulated to be 0.5 g L^{-1}.

In general, pH is a key factor affecting the removal of STZ in wastewater. Under different pH conditions (Fig. 4b), 2K-SBC exhibited different STZ adsorption capacities, indicating that the

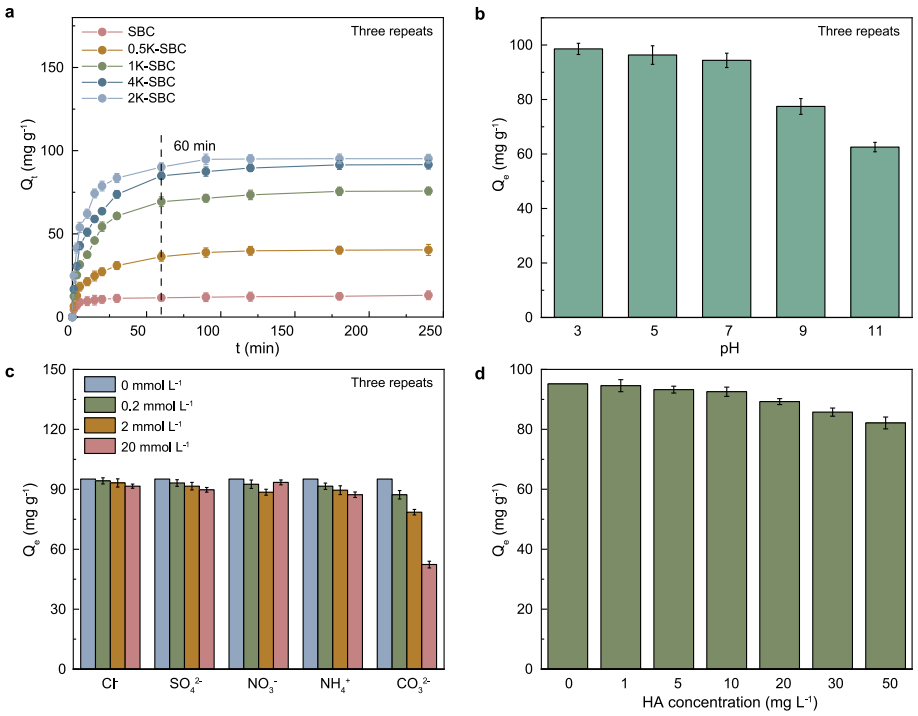

Fig. 4. Effects of contact time (**a**) on the adsorption performance of SBC and KSBC (C_{STZ} = 50 mg L^{-1}, $C_{adsorbent}$ = 0.5 g L^{-1}, pH = 7 and T = 25 °C). Effects of pH (**b**) on the adsorption performance of 2K-SBC (C_{STZ} = 50 mg L^{-1}, $C_{adsorbent}$ = 0.5 g L^{-1} and T = 25 °C). Effects of anionic species and strength (**c**) on the adsorption performance of 2K-SBC (C_{STZ} = 50 mg L^{-1}, $C_{adsorbent}$ = 0.5 g L^{-1}, pH = 7 and T = 25 °C). Effects of humid acid concentration (**d**) on the adsorption performance of 2K-SBC (C_{STZ} = 50 mg L^{-1}, $C_{adsorbent}$ = 0.5 g L^{-1}, pH = 7 and T = 25 °C).

existing form of STZ in an aqueous solution was closely related to pH value [41]. As displayed by the results presented in Table S2, STZ is an ionic polar organic compound with two acid dissociation constants (pK_{a1} = 2.2 and pK_{a2} = 7.24). Therefore, the state of STZ in an aqueous solution is different for different pH conditions. Under the pH < 2.2, 2.2 < pH < 7.24 and pH > 7.24, STZ mainly existed in the form of cations (STZ^+), neutral molecules (STZ^0) and anionic species (STZ^-), respectively. The pH_{ZpC} value of 2K-SBC was 6.67 (Fig. S4). Therefore, when the solution pH was lower than their pH_{PZC}, 2K-SBC was protonated and had a positive surface charge, otherwise, it was negatively charged. When the pH lay within the range of 3–7, most STZ would exist in the form of STZ^0, whereas the electrostatic interaction would occur with the surface of the charged 2K-SBC, thereby greatly enhancing the adsorption of STZ onto 2K-SBC. When the pH value lay within the range of 9–11, most STZ would exist in the form of STZ^-, and the electrostatic repulsion would occur with the surface of negatively charged 2K-SBC, thereby weakening the adsorption of STZ onto 2K-SBC. However, even at the pH of 11, the adsorption capacity of 2K-SBC for STZ was still as high as 62.54 mg g^{-1}, indicating that other adsorption mechanisms (such as pore filling, π-π EDA interaction, and hydrogen bonding) also determined the adsorption of STZ onto 2K-SBC.

Electrolytic ions existing in natural waters would usually compete with the antibiotic molecules to occupy the adsorption sites of an adsorbent, leading to a decrease in the adsorption performance of the material. In the current work, Cl^-, SO_4^{2-}, NO_3^-, NH_4^+, and CO_3^{2-} were selected to simulate the electrolytic ions existing in water bodies. The interference in the adsorption capacity of 2K-SBC due to different electrolytic ions was studied (Fig. 4c**).** Apart from CO_3^{2-}, the interference of other electrolytic ions in the adsorption of STZ was nearly negligible. This may illustrate that, after hydrolysis, CO_3^{2-} would generate OH^-, which increased the pH value of the solution ($CO_3^{2-} + H_2O \rightarrow HCO_3^- + OH^-$), resulting in a decrease in the adsorption capacity of 2K-SBC.

In addition to the electrolytic ions, HA was also selected to simulate the anti-interference capability of 2K-SBC to natural organic matter. Humic acid levels in common surface waters lay within the range of 1–5 mg L^{-1}, whereas in some places, the HA content can reach 10 mg L^{-1} or even higher [42]. Obviously, a low concentration of HA had nearly no effect on the adsorption of STZ, as the concentration of HA exceeded the value of 20 mg L^{-1} (Fig. 4d), the adsorption capacity of 2K-SBC for STZ decreased slightly. This may because HA is weakly alkaline, which increased the pH of the reaction solution, thereby weakening the adsorption of STZ. Overall, 2K-SBC showed an excellent anti-interference capability towards HA, indicating its high potential in practical applications.

3.3. Adsorption kinetics, isotherm, and thermodynamics analysis

The adsorption process of STZ in SBC and 2K-SBC was studied through the pseudo-first-order (PFO) and pseudo-second-order (PSO) kinetic models. Table 1 specifically records the corresponding kinetic parameters (K_1, K_2, R^2, and q_e). The correlation coefficients (R^2) of PSO kinetics models of SBC and 2K-SBC were

Table 1
Parameters of PFO and PSO kinetic models for STZ adsorption by SBC and 2K-SBC.

Models	Parameters	SBC	2K-SBC
	Experimental q_e (mg g^{-1})	13.08	95.21
Pseudo-first-order	q_e (mg g^{-1})	11.54	90.34
	K_1 (min^{-1})	0.03310	0.1532
	R^2	0.9291	0.9483
Pseudo-second-order	q_e (mg g^{-1})	11.75	96.61
	K_2 (g mg^{-1} min^{-1}))	0.07852	0.00254
	R^2	0.9912	0.9943

determined to be 0.9912 and 0.9943, while the R^2 of the PFO kinetics models were found to be 0.9291 and 0.9483, respectively. Obviously, the PSO kinetic model better fitted the adsorption data of SBC and 2K-SBC (Fig. 5a). More importantly, based on the PSO kinetics model, the theoretical adsorption capacities of SBC and 2K-SBC approached the actual adsorption capacities, which further exhibited that the adsorption behavior was better represented by the PSO kinetic model.

Generally, the adsorption process has three stages: the transportation of adsorbate from the bulk solution to the surface of adsorbent, film diffusion, and intra-particle diffusion. The fitting results of the intra-particle diffusion models of SBC and 2K-SBC are shown in Fig. 5b. The data corresponding to the SBC and 2K-SBC's intra-particle diffusion models did not pass through the origin, indicating that intra-particle diffusion was not the only rate-limiting step in the adsorption process [20]. However, the difference was that STZ's adsorption on 2K-SBC could be divided into three stages (I, II, and III), while the process of STZ's adsorption on SBC was divided into only two stages (I and III). Stage I, II, and III represented film diffusion, intra-particle diffusion, and the equilibrium stage, respectively. These results indicate that both the film diffusion and the intra-particle diffusion could affect the rate of adsorption of STZ onto 2K-SBC, while intra-particle diffusion had almost no effect on the adsorption of STZ onto SBC. This can further prove that many holes produced by $KHCO_3$ could largely enhance the diffusion of STZ into the particles inside KSBC .

The Langmuir and Freundlich models were employed to further understand the adsorption behavior of STZ on 2K-SBC. The corresponding fitting results are shown in Fig. 5c. The R^2 values of the Langmuir model at different temperatures (298, 308, and 318K) were greater than those of the Freundlich model (Table 2), indicating that the 2K-SBC adsorption was fitted more appropriately using the Langmuir model. Similarly, the adsorption model of SBC is more consistent with the Langmuir model (Fig. S5 and Table S3). Moreover, the amount of adsorption at the adsorption equilibrium was inversely proportional to temperature, demonstrating that high temperature may inhibit the adsorption process to a certain extent.

Table 2
Parameters of Langmuir and Freundlich models for STZ adsorption by 2K-SBC at different temperature.

Models	Parameters	298 K	308 K	318 K
Langmuir	q_m (mg g^{-1})	218.4	209.3	200.9
	K_L (L mg^{-1})	0.3794	0.3931	0.4212
	R^2	0.9943	0.9892	0.9910
Freundlich	K_F (L g^{-1})	109.5	108.3	108.0
	1/n	0.1610	0.1541	0.1421
	R^2	0.9242	0.9163	0.9130

The direction and driving force in the adsorption process of STZ using 2K-SBC were studied using the adsorption thermodynamic analysis. The corresponding parameters (ΔG°, ΔH°, and ΔS°) can be obtained by plotting the reciprocal of the corresponding temperature (1/T) against the -lnK_d (Fig. 5d). Table 3 specifically records the adsorption thermodynamic parameters of STZ onto 2K-SBC. The ΔG° values calculated under various temperatures were all negative, manifesting that the adsorption process was spontaneous. Further analysis showed that the increase in temperature would lead to the increase in ΔG°, whereas high temperature would inhibit the spontaneous reaction to some extent [43,44]. In addition, the ΔH° < 0 confirmed that the adsorption process of STZ onto 2K-SBC was a spontaneous exothermic process. Meanwhile, ΔS° < 0 revealed that the adsorption process involved entropy reduction.

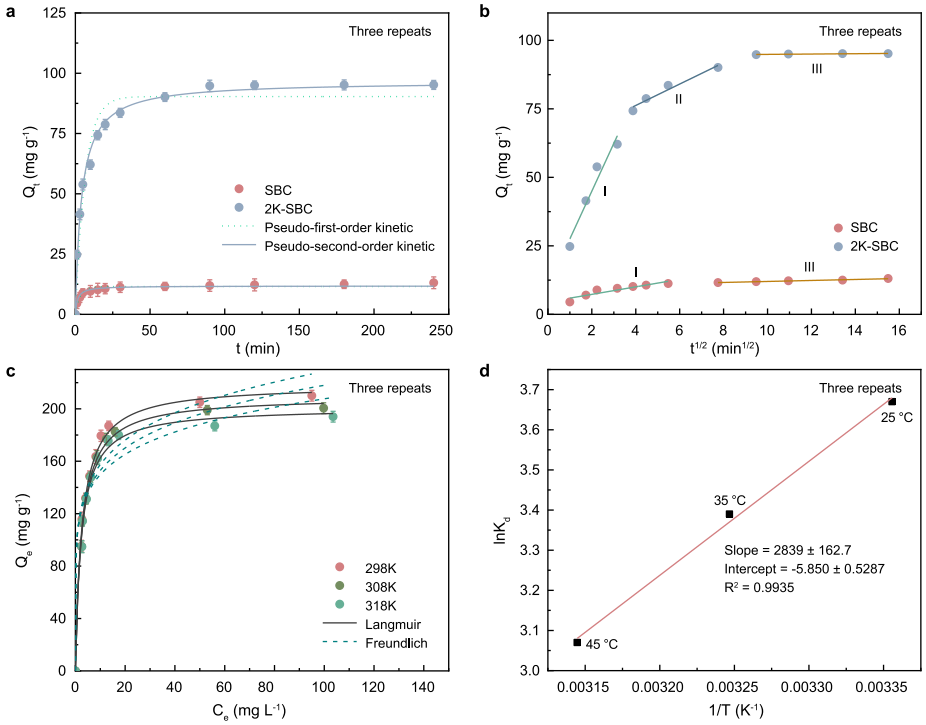

Fig. 5. Adsorption kinetic (**a**) for STZ adsorption onto SBC and 2K-SBC (C_{STZ} = 50 mg L^{-1}, $C_{adsorbent}$ = 0.5 g L^{-1}, pH = 7 and T = 25 °C). Intra-particle diffusion model (**b**) for STZ adsorption onto 2K-SBC (C_{STZ} = 50 mg L^{-1}, $C_{adsorbent}$ = 0.5 g L^{-1}, pH = 7 and T = 25 °C. Adsorption Isotherm (**c**) for STZ adsorption onto 2K-SBC (C_{STZ} = 50–200 mg L^{-1}, $C_{adsorbent}$ = 0.5 g L^{-1}, pH = 7 and T = 25, 35 and 45 °C). Plot of ln(K_d) versus 1/T (**d**) for STZ adsorption onto 2K-SBC (C_{STZ} = 50 mg L^{-1}, $C_{adsorbent}$ = 0.5 g L^{-1}, pH = 7 and T = 25, 35 and 45 °C).

Table 3
Parameters of thermodynamic models for STZ adsorption by 2K-SBC at different temperatures.

	Parameters	K_d (L g^{-1})	lnK_d	ΔG° (kJ mol^{-1})	ΔH° (kJ mol^{-1})	ΔS° (kJ mol^{-1} K^{-1})
Temperature (K)	298 K	39.32	3.672	−9.130	−23.61	−0.04860
	308 K	30.25	3.409	−8.640		
	318 K	21.53	3.069	−8.160		

3.4. Stability and reusability of the adsorbent

In order to explore the reusability of 2K-SBC, the contaminants attached to the surface and the pore diameter of 2K-SBC were removed by high-temperature pyrolysis. As shown in Fig. S6, after four regeneration cycles, the removal rate of STZ by 2K-SBC decreased from 95.21% to 80.38%, which indicated that 2K-SBC can be recycled through thermal regeneration methods. The fine regeneration performance of 2K-SBC indicated that the material can be used as an efficient and promising adsorbent.

3.5. Possible adsorption mechanisms

The adsorption mechanism of pollutants on biochar includes pore filling, electrostatic interaction, π-π EDA interaction, and hydrogen bonding [32,45–48]. The dominant mechanism is determined by the properties of biochar and the specific solution conditions. In this study, the adsorption mechanisms were confirmed via correlation analysis and characterization (Scheme 1).

First, the adsorption capacity and SSA were satisfactorily fitted ($R^2 = 0.952$) (Fig. S7), proving that pore filling may be the principal mechanism for the adsorption of STZ onto 2K-SBC [20,49]. After the adsorption of STZ, the BET and pore volume of 2K-SBC were measured to further demonstrate this inference (Table S4). Both the BET and total pore volume of biochar after STZ adsorption dramatically decreased, indicating that STZ had occupied the available sorption sites in 2K-SBC and that many channels in the biochar had been plugged. This analysis revealed that the adsorption of STZ occurred largely on the external surface and pores of 2K-SBC, implying that the pore filling effect was the major mechanism for STZ's adsorption on 2K-SBC. Second, based upon the effect of pH value on the adsorption of STZ, the contribution of electrostatic interaction in the adsorption process can be highlighted (Fig. 4b). Third, after the adsorption of STZ, the FTIR spectra of 2K-SBC were employed to illustrate the contribution of π-π EDA interactions and hydrogen bonding in the adsorption process. As shown in Fig. S8, after the adsorption of STZ onto 2K-SBC, the position of the C=C functional group deviated marginally from 1625 to 1587 cm^{-1}, exhibiting that the π-π EDA interactions occurred during the adsorption process [50]. Similarly, the −OH peak at 3441 cm^{-1} of 2K-SBC was slightly off-set to 3460 cm^{-1} after the adsorption of STZ, illustrating that the −OH could interact with O and N atoms in STZ through hydrogen bonding to promote the adsorption process [51]. However, the slight shift of C=C and −OH peaks suggested that π-π EDA interactions and hydrogen bonding may not be the main mechanism for the adsorption of STZ onto 2K-SBC. Based on the above analysis, pore filling and electrostatic interactions were determined to be the main mechanisms for the adsorption of STZ onto 2K-SBC, followed by π-π EDA interactions and hydrogen bonding.

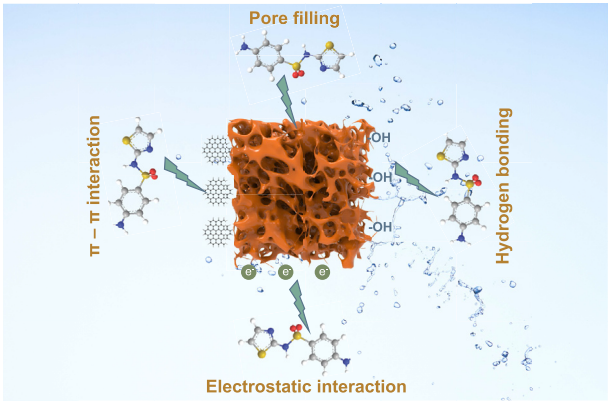

Scheme 1. Probable adsorption mechanism of KSBC.

4. Conclusion

Designing a green adsorbent with a tremendous amount of meso-/micro-pores is of great importance. Inspired by the cheese-making process, $KHCO_3$ was selected as the activator, and a novel *Spirulina* residue-derived cheese-like porous KSBC was prepared. The results showed that the introduction of $KHCO_3$ can dramatically affect the adsorption of STZ by affecting the specific surface area and pore volume of SBC. The 2K-SBC sample could achieve the optimum removal of STZ (95.21%), with a maximum adsorption capacity of 218.40 mg g^{-1}. Moreover, the excellent and stable regeneration of 2K-SBC (>83%) was verified by four consecutive adsorption-desorption cycles. Compared with the recent work on other carbon-based adsorbents (Table S5), this work achieved a better adsorption capacity for STZ in water bodies. Furthermore, the possible adsorption mechanism for STZ was discussed in depth. This study not only provides technical guidance for the preparation of efficient and environment-friendly porous biochar, but also offers a solid theoretical basis for the use of KSBC to remove antibiotics from wastewaters.

Declaration of competing interest

The authors declare that they have no known competing financial interests or personal relationships that could have appeared to influence the work reported in this paper.

Acknowledgements

This work was financially supported by the following funding: National Natural Science Foundation of China (No. 52070057 and No. 51961165104), Project of a Thousand Youth Talents (No. AUGA2160100917), and Open Project of State Key Laboratory of Urban Water Resource and Environment, Harbin Institute of Technology (No. 2019DX09).

Appendix A. Supplementary data

Supplementary data to this article can be found online at https://doi.org/10.1016/j.ese.2022.100168.

References

[1] B. Yang, X. Cheng, Y. Zhang, W. Li, J. Wang, H. Guo, Insight into the role of binding interaction in the transformation of tetracycline and toxicity distribution, Environ. Sci. Ecotechnol. 8 (2021) 100127.

[2] Y. Wang, Y. Yang, X. Liu, J. Zhao, R. Liu, B. Xing, Interaction of microplastics with antibiotics in aquatic environment: distribution, adsorption, and toxicity, Environ. Sci. Technol. 55 (2021) 15579–15595.

[3] B. Yang, X. Cheng, Y. Zhang, W. Li, J. Wang, H. Guo, Probing the roles of pH and ionic strength on electrostatic binding of tetracycline by dissolved organic matters: reevaluation of modified fitting model, Environ. Sci. Ecotechnol. 8 (2021) 100133.

[4] S. Li, C. Zhang, F. Li, T. Hua, Q. Zhou, S.-H. Ho, Technologies towards antibiotic resistance genes (ARGs) removal from aquatic environment: a critical review, J. Hazard Mater. 411 (2021) 125148.

[5] J. Li, L. Zhao, M. Feng, C.-H. Huang, P. Sun, Abiotic transformation and ecotoxicity change of sulfonamide antibiotics in environmental and water treatment processes: a critical review, Water Res. 202 (2021) 117463.

[6] A. Almajed, M. Ahmad, A.R.A. Usman, M.I. Al-Wabel, Fabrication of sand-based novel adsorbents embedded with biochar or binding agents via calcite precipitation for sulfathiazole scavenging, J. Hazard Mater. 405 (2021) 124249.

[7] Y.-d. Chen, X. Duan, X. Zhou, R. Wang, S. Wang, N.-q. Ren, S.-H. Ho, Advanced oxidation processes for water disinfection: features, mechanisms and prospects, Chem. Eng. J. 409 (2021) 128207.

[8] H. Song, L. Yan, J. Jiang, J. Ma, S. Pang, X. Zhai, W. Zhang, D. Li, Enhanced degradation of antibiotic sulfamethoxazole by electrochemical activation of PDS using carbon anodes, Chem. Eng. J. 344 (2018) 12–20.

[9] S. Wang, R. Yuan, H. Chen, F. Wang, B. Zhou, Anaerobic biodegradation of four sulfanilamide antibiotics: kinetics, pathways and microbiological studies, J. Hazard Mater. 416 (2021) 125840.

[10] S.-H. Ho, Y.-d. Chen, Z.-k. Yang, D. Nagarajan, J.-S. Chang, N.-q. Ren, High-efficiency removal of lead from wastewater by biochar derived from anaerobic digestion sludge, Bioresour. Technol. 246 (2017) 142–149.

[11] X. Han, W. Wang, X. Ma, Adsorption characteristics of methylene blue onto low cost biomass material lotus leaf, Chem. Eng. J. 171 (2011) 1–8.

[12] Y.-d. Chen, R. Wang, X. Duan, S. Wang, N.-q. Ren, S.-H. Ho, Production, properties, and catalytic applications of sludge derived biochar for environmental remediation, Water Res. 187 (2020) 116390.

[13] J. Peng, Y. He, C. Zhou, S. Su, B. Lai, The carbon nanotubes-based materials and their applications for organic pollutant removal: a critical review, Chin. Chem. Lett. 32 (2021) 1626–1636.

[14] X. Weng, Z. Lin, X. Xiao, C. Li, Z. Chen, One-step biosynthesis of hybrid reduced graphene oxide/iron-based nanoparticles by eucalyptus extract and its removal of dye, J. Clean. Prod. 203 (2018) 22–29.

[15] X.-F. Tan, S.-S. Zhu, R.-P. Wang, Y.-D. Chen, P.-L. Show, F.-F. Zhang, S.-H. Ho, Role of biochar surface characteristics in the adsorption of aromatic compounds: pore structure and functional groups, Chin. Chem. Lett. 32 (2021) 2939–2946.

[16] R. Crisafully, M.A.L. Milhome, R.M. Cavalcante, E.R. Silveira, D. De Keukeleire, R.F. Nascimento, Removal of some polycyclic aromatic hydrocarbons from petrochemical wastewater using low-cost adsorbents of natural origin, Bioresour. Technol. 99 (2008) 4515–4519.

[17] Z. Yin, C. Cui, H. Chen, Duoni, X. Yu, W. Qian, The application of carbon nanotube/graphene-based nanomaterials in wastewater treatment, Small 16 (2020) 1902301.

[18] M.D. Faysal Hossain, N. Akther, Y. Zhou, Recent advancements in graphene adsorbents for wastewater treatment: current status and challenges, Chin. Chem. Lett. 31 (2020) 2525–2538.

[19] R. Zhang, X. Zheng, B. Chen, J. Ma, X. Niu, D. Zhang, Z. Lin, M. Fu, S. Zhou, Enhanced adsorption of sulfamethoxazole from aqueous solution by Fe-impregnated graphited biochar, J. Clean. Prod. 256 (2020) 120662.

[20] X. Zhang, D.D. Gang, J. Zhang, X. Lei, Q. Lian, W.E. Holmes, M.E. Zappi, H. Yao, Insight into the activation mechanisms of biochar by boric acid and its application for the removal of sulfamethoxazole, J. Hazard Mater. 424 (2022) 127333.

[21] X.-f. Tan, S.-b. Liu, Y.-g. Liu, Y.-l. Gu, G.-m. Zeng, X.-j. Hu, X. Wang, S.-h. Liu, L.-h. Jiang, Biochar as potential sustainable precursors for activated carbon production: multiple applications in environmental protection and energy storage, Bioresour. Technol. 227 (2017) 359–372.

[22] S. Hadi, E. Taheri, M.M. Amin, A. Fatehizadeh, T.M. Aminabhavi, Adsorption of 4-chlorophenol by magnetized activated carbon from pomegranate husk using dual stage chemical activation, Chemosphere 270 (2021) 128623.

[23] F. Guo, K. Peng, S. Liang, X. Jia, X. Jiang, L. Qian, Evaluation of the catalytic performance of different activated biochar catalysts for removal of tar from biomass pyrolysis, Fuel 258 (2019) 116204.

[24] Y. Wang, W. Zhao, W. Zheng, S. Chen, J. Zhao, Preparation of N-doped carbon nanosheets from sewage sludge for adsorption studies of Cr(VI) from aqueous solution, Nanomaterials (2019) 9.

[25] J. Shin, Y.-G. Lee, S.-H. Lee, S. Kim, D. Ochir, Y. Park, J. Kim, K. Chon, Single and competitive adsorptions of micropollutants using pristine and alkali-modified biochars from spent coffee grounds, J. Hazard Mater. 400 (2020) 123102.

[26] Z. Meng, Y. Liu, X. Li, Z. Ma, Removal of siloxane (L2) from biogas using methyl-functionalised silica gel as adsorbent, Chem. Eng. J. 389 (2020) 124440.

[27] J. Qiu, H. Hou, S. Liang, L. Yang, Q. Gan, S. Tao, W. Yu, R. Lv, L. Ding, K. Xiao, J. Hu, B. Liu, J. Yang, Hierarchically porous biochar preparation and simultaneous nutrient recovery from sewage sludge via three steps of alkali-activated pyrolysis, water leaching and acid leaching, Resour. Conserv. Recycl. 176 (2022) 105953.

[28] J. Zhang, J. Shao, Q. Jin, X. Zhang, H. Yang, Y. Chen, S. Zhang, H. Chen, Effect of deashing on activation process and lead adsorption capacities of sludge-based biochar, Sci. Total Environ. 716 (2020) 137016.

[29] H.N. Tran, F. Tomul, N. Thi Hoang Ha, D.T. Nguyen, E.C. Lima, G.T. Le, C.-T. Chang, V. Masindi, S.H. Woo, Innovative spherical biochar for pharmaceutical removal from water: insight into adsorption mechanism, J. Hazard Mater. 394 (2020) 122255.

[30] X. He, J. Li, Q. Meng, Z. Guo, H. Zhang, Y. Liu, Enhanced adsorption capacity of sulfadiazine on tea waste biochar from aqueous solutions by the two-step sintering method without corrosive activator, J. Environ. Chem. Eng. 9 (2021) 104898.

[31] A. Jain, D.R. Peshwe, A. Kumar, S.J. Dhoble, M.M. Yerpude, G.B. Nair, H.C. Swart, Theoretical analysis of electron vibration interactions and study of photo physical properties in Ce^{3+} doped $Ca_2P_2O_7$ nano phosphor capped with SHMP, Mater. Chem. Phys. 196 (2017) 213–221.

[32] B. Li, Y. Huang, Z. Wang, J. Li, Z. Liu, S. Fan, Enhanced adsorption capacity of tetracycline on tea waste biochar with $KHCO_3$ activation from aqueous solution, Environ. Sci. Pollut. Res. 28 (2021) 44140–44151.

[33] J. Liao, L. Ding, Y. Zhang, W. Zhu, Efficient removal of uranium from wastewater using pig manure biochar: understanding adsorption and binding mechanisms, J. Hazard Mater. 423 (2022) 127190.

[34] L. Liu, J. Zhao, X. Liu, S. Bai, H. Lin, D. Wang, Reduction and removal of As(V) in aqueous solution by biochar derived from nano zero-valent-iron (nZVI) and sewage sludge, Chemosphere 277 (2021) 130273.

[35] G. Bottari, M.Á. Herranz, L. Wibmer, M. Volland, L. Rodríguez-Pérez, D.M. Guldi, A. Hirsch, N. Martín, F. D'Souza, T. Torres, Chemical functionalization and characterization of graphene-based materials, Chem. Soc. Rev. 46 (2017) 4464–4500.

[36] J.-B. Wu, M.-L. Lin, X. Cong, H.-N. Liu, P.-H. Tan, Raman spectroscopy of graphene-based materials and its applications in related devices, Chem. Soc. Rev. 47 (2018) 1822–1873.

[37] S.-H. Ho, Y.-d. Chen, R. Li, C. Zhang, Y. Ge, G. Cao, M. Ma, X. Duan, S. Wang, N.-q. Ren, N-doped graphitic biochars from C-phycocyanin extracted Spirulina residue for catalytic persulfate activation toward nonradical disinfection and organic oxidation, Water Res. 159 (2019) 77–86.

[38] Y.-d. Chen, X. Duan, C. Zhang, S. Wang, N.-q. Ren, S.-H. Ho, Graphitic biochar catalysts from anaerobic digestion sludge for nonradical degradation of micropollutants and disinfection, Chem. Eng. J. 384 (2020) 123244.

[39] P. Zhang, X. Wang, B. Xue, P. Huang, Y. Hao, J. Tang, S.P. Maletić, S.D. Rončević, H. Sun, Preparation of graphite-like biochars derived from straw and newspaper based on ball-milling and TEMPO-mediated oxidation and their supersorption performances to imidacloprid and sulfadiazine, Chem. Eng. J. 411 (2021) 128502.

[40] S. Zhang, J. Feng, J. Feng, Y. Jiang, F. Ding, Carbon aerogels by pyrolysis of TEMPO-oxidized cellulose, Appl. Surf. Sci. 440 (2018) 873–879.

[41] Y. Wang, W.-B. Jiao, J.-T. Wang, G.-F. Liu, H.-L. Cao, J. Lü, Amino-functionalized biomass-derived porous carbons with enhanced aqueous adsorption affinity and sensitivity of sulfonamide antibiotics, Bioresour. Technol. 277 (2019) 128–135.

[42] N. Li, H.K. Lee, Solid-phase extraction of polycyclic aromatic hydrocarbons in surface water: negative effect of humic acid, J. Chromatogr. A 921 (2001) 255–263.

[43] W.A. Shaikh, S. Chakraborty, R.U. Islam, A.A. Ghfar, M. Naushad, J. Bundschuh, J.P. Maity, N.K. Mondal, Fabrication of biochar-based hybrid Ag nanocomposite from algal biomass waste for toxic dye-laden wastewater treatment, Chemosphere 289 (2022) 133243.

[44] V.R. Moreira, Y.A.R. Lebron, L.C. Lange, L.V.S. Santos, Simultaneous biosorption of Cd(II), Ni(II) and Pb(II) onto a brown macroalgae Fucus vesiculosus: mono- and multi-component isotherms, kinetics and thermodynamics, J. Environ. Manag. 251 (2019) 109587.

[45] A.S. Abdulhameed, N.N.M. Firdaus Hum, S. Rangabhashiyam, A.H. Jawad, L.D. Wilson, Z.M. Yaseen, A.A. Al-Kahtani, Z.A. Alothman, Statistical modeling and mechanistic pathway for methylene blue dye removal by high surface area and mesoporous grass-based activated carbon using K2CO3 activator, J. Environ. Chem. Eng. 9 (2021) 105530.

[46] A.H. Jawad, M. Bardhan, M.A. Islam, M.A. Islam, S.S.A. Syed-Hassan, S.N. Surip, Z.A. Alothman, M.R. Khan, Insights into the modeling, characterization and adsorption performance of mesoporous activated carbon from corn cob residue via microwave-assisted H3PO4 activation, Surface. Interfac. 21 (2020) 100688.

[47] A.H. Jawad, A. Saud Abdulhameed, L.D. Wilson, S.S.A. Syed-Hassan, Z.A. Alothman, M. Rizwan Khan, High surface area and mesoporous activated carbon from KOH-activated dragon fruit peels for methylene blue dye adsorption: optimization and mechanism study, Chin. J. Chem. Eng. 32 (2021) 281–290.

[48] A.H. Jawad, A.S. Abdulhameed, M.A.K.M. Hanafiah, Z.A. Alothman, M.R. Khan, S.N. Surip, Numerical desirability function for adsorption of methylene blue dye by sulfonated pomegranate peel biochar: modeling, kinetic, isotherm, thermodynamic, and mechanism study, Kor. J. Chem. Eng. 38 (2021) 1499–1509.

[49] B. Li, Y. Zhang, J. Xu, Z. Xie, J. Tang, X. Li, S. Fan, Simultaneous carbonization, activation, and magnetization for producing tea waste biochar and its application in tetracycline removal from the aquatic environment, J. Environ. Chem. Eng. 9 (2021) 105324.
[50] Q. Wu, Y. Zhang, M.-h. Cui, H. Liu, H. Liu, Z. Zheng, W. Zheng, C. Zhang, D. Wen, Pyrolyzing pharmaceutical sludge to biochar as an efficient adsorbent for deep removal of fluoroquinolone antibiotics from pharmaceutical wastewater: performance and mechanism, J. Hazard Mater. (2021) 127798.
[51] J. Zhao, G. Liang, X. Zhang, X. Cai, R. Li, X. Xie, Z. Wang, Coating magnetic biochar with humic acid for high efficient removal of fluoroquinolone antibiotics in water, Sci. Total Environ. 688 (2019) 1205–1215.